Basement sliding and the formation of fault systems on Mt. Etna volcano

John Murray, Benjamin van Wyk de Vries

Journal of Volcanology and Geothermal Research 428 (2022) 107573

Contents lists available at ScienceDirect

Journal of Volcanology and Geothermal Research

journal homepage: www.journals.elsevier.com/journal-of-volcanology-and-geothermal-research

Basement sliding and the formation of fault systems on Mt. Etna volcano

John B. Murray [a,*], Benjamin van Wyk de Vries [b]

[a] School of Environment, Earth & Ecosystem Sciences, The Open University, Walton Hall, Milton Keynes, MK7 6AA, United Kingdom
[b] Université Clermont-Auvergne, CNRS-UMR6524, IRD, OPGC, Laboratoire Magmas et Volcans, 6 avenue Blaise Pascal, 63178 Aubière, France

ARTICLE INFO

Keywords:
Volcano Tectonics
Gravitational spreading
Etna volcano
Basement sliding
Volcano instability
Eruption mechanism
Faulting

ABSTRACT

The influence of faulting on the eruptive mechanisms of Mt. Etna has been intensively studied, especially regarding the importance of regional tectonics, magma pressure, gravitational spreading and east flank instability. Here we examine the influence of an additional process: the wholesale sliding of the Etna massif along its sloping basement (Murray et al., 2018). Using laboratory analogue experiments, we create a series of model volcanoes on sloping basements, with obstructions to represent the mountains and hills surrounding Etna, and an unconstrained downslope edge to represent the unbuttressed seaward slopes. We find that analogues of all the Etna fault systems can be produced in the same model. Furthermore, we find that the relative velocities of transcurrent faulting and extension of each model flank fault system match those of Mt. Etna in every case. We also find convincing evidence that gravitational spreading of the summit cone, combined with downslope sliding, controls the position of future eruptive vents around the summit, by creating faults and fractures that form paths of least resistance for magma intrusions (Pezzo et al., 2020). The intruding magma in turn augments fracture opening by an order of magnitude, in a feedback process that dominates within the north-south summit graben. We conclude that gravitational spreading and sliding are the dominant processes in creating faults at Etna, and that these two processes, augmented by magma pressure, are responsible for the rapid seaward movement of the eastern slopes, tectonically cut off from the western flanks by the summit graben. The influence of regional tectonism is up to two orders of magnitude lower. The conceptual model derived here could make an important contribution to the investigation and monitoring of eruptive, seismic and landslide hazards, by providing a unified mechanical system that can be used to understand deformation.

1. Introduction

The flanks of Mt. Etna are dissected by large numbers of active fault systems, particularly on the eastern side of the volcano. These faults are key to understanding the tectonic and eruptive mechanisms of one of the world's most active volcanoes. In the past, the disposition of Etna faults were ascribed to stress regimes associated with the regional tectonic setting of eastern Sicily (Rittmann, 1973; Grindley, 1973; Lo Giudice et al., 1982). More recently, the effect of magma pressure accompanying dyke intrusion over a long period has been recognised (Walker, 1992; Tibaldi and Gropelli, 2002; Solaro et al., 2010; Murray, 2019). The advent of gravitational spreading as a major volcanic process (Borgia et al., 1992; Borgia, 1994) and the recognition of the east flank instability of Etna (Murray et al., 1994; Rasá et al., 1996; Rust and Neri, 1996; Acocella et al., 2013; Urlaub et al., 2018) has led to greater understanding of how these faults are related to gravitational stresses induced as the Etna edifice deforms under its own weight.

In this paper, we consider the additional effect of the downslope sliding of the entire massif of Etna between major eruptions (Murray et al., 2018). This was a new discovery based on 20 years of deformation data, that explained the asymmetrical horizontal displacement vectors of nearly 100 GPS stations all over Mt. Etna that preceded all major eruptions, and accounted for the off-centre radial expansion centre. Previous ideas of the asymmetry had presented ad hoc models invoking large scale dislocation planes beneath the volcano that differed in number, size, position, direction of displacement, shape and depth from model to model and from eruption to eruption, and resulted in mainly poor fits to data. For example, to explain displacements 1994–1995 that preceded the 2001 flank eruption, Bonforte and Puglisi (2003) proposed 3 huge sloping dislocation planes moving in different directions, comprising rectangles with sides up to 28 km, at 0 km, 1.2 km and 3.4 km beneath sea level, situated southeast and south of the summit, and dipping 88° east, 19° east and 18° west respectively. To account for horizontal displacement vectors 2003–2004 preceding the 2004–5

* Corresponding author.
E-mail address: j.b.murray@open.ac.uk (J.B. Murray).

https://doi.org/10.1016/j.jvolgeores.2022.107573
Received 16 December 2021; Received in revised form 7 April 2022; Accepted 6 May 2022
Available online 14 May 2022

eruption, Bonaccorso et al. (2006) proposed a single large 20 × 25 km rectangular dislocation to the east, dipping 11° ESE and centred at the Ionian shoreline at 0 to 1 km depth. But when modelling the association of the Pernicana fault displacements with eruptions between 1980 and 2010, Bonaccorso et al. (2013) used a much deeper and smaller rectangular dislocation plane 7 × 8 km at 4 km below sea level but centred 16 km from the shoreline. None of the proposed different sloping dislocation planes proposed by these authors corresponded to any known geological boundary.

The fact that pre-eruption vectors radiate not from the summit but a few km upslope has led to suggestions that the magma chamber is up to 4 km WNW of the summit, or that it is tall and slopes in this direction (Puglisi et al., 2004; Bonaccorso et al., 2011). In both these cases the position of the magma chamber contradicted that of the geological evidence (Branca et al., 2011a).

All these inconsistencies were neatly explained by one unifying model: that between big eruptions, Etna slides downslope on its ductile sedimentary basement, at a rate measured at 10 ± 7 mm y^{-1} in 2001–2002, 17 ± 5 mm y^{-1} in 2003–2004, 11 ± 5 mm y^{-1} in 2005–2007 and 16 ± 3 mm y^{-1} in 2008–2012. These sliding rates do not differ significantly from each other, and result in a weighted mean value for downslope sliding of 14 ± 4 mm y^{-1} in a direction of 120° ±15°. (Murray et al., 2018). Once the sliding rate is measured and a correction applied to the precursive deformation data, surface expansion vectors radiate from the summit, in line with other evidence, and vectors are of symmetrical length on all sides of the volcano, with consistently low O—C values. Also, the sliding takes place at the same well-defined geological dichotomy (in fact the only well-defined geological dichotomy beneath Etna) in each case.

Here, we create a mechanical analogue model set that incorporates the structural environment of Etna (its edifice, the substratum, and bounding mountains and coastal conditions) and produces faults

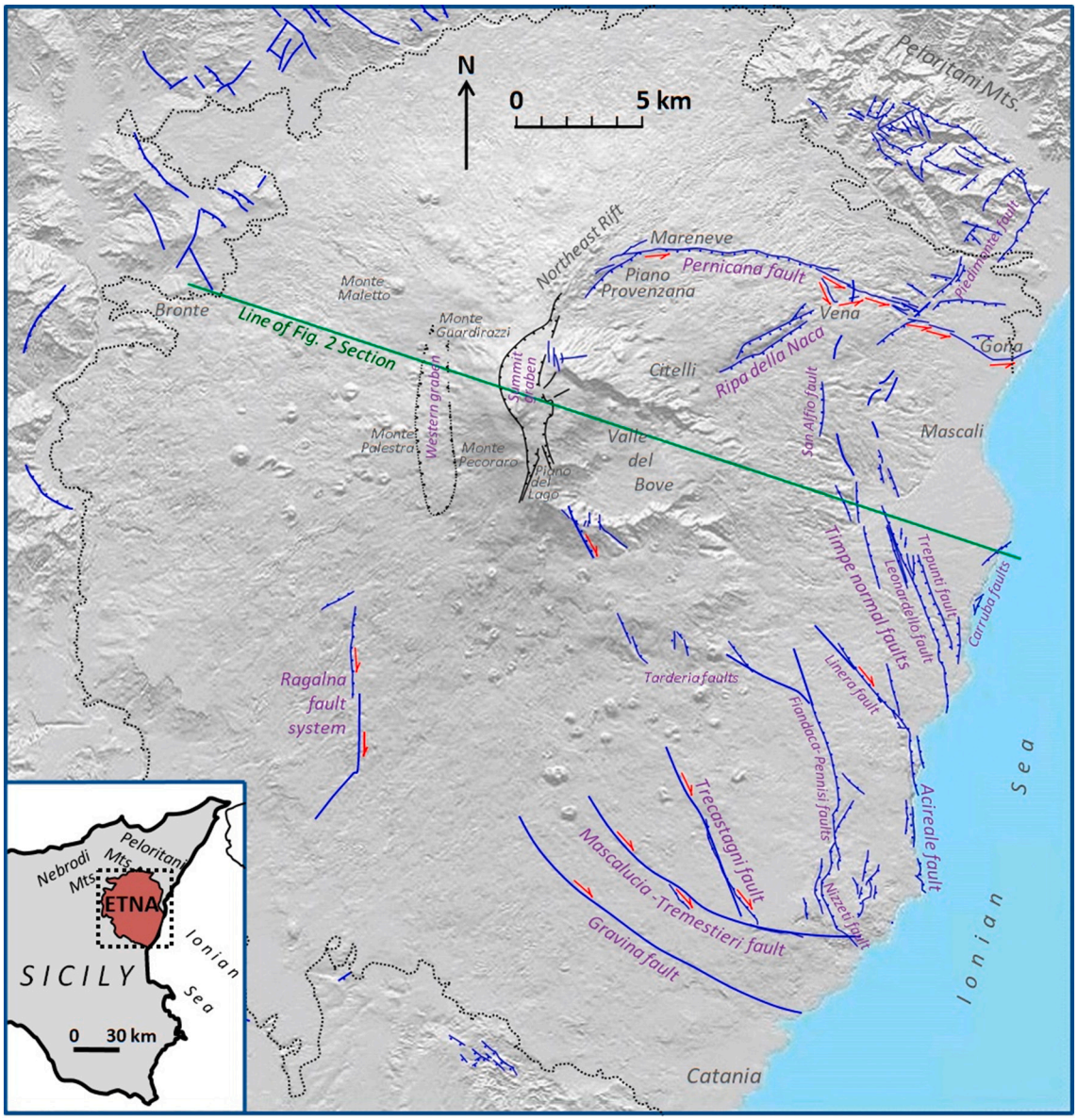

Fig. 1. Map of the faults of Mt. Etna and its immediate surroundings, based on maps in Rust and Neri, 1996, Rasá et al., 1996, Monaco et al., 1997, Froger et al., 2001, Neri et al., 2004, Branca et al., 2011a, and Murray, 2019. Blue lines are the faults, with ticks on the downthrow side, and black lines the bounding faults of the summit graben. The hachured dotted lines west of the summit graben depict the extent of a hitherto undescribed area of subsidence and lateral extension, here named the Western Graben. Red arrows indicate the direction of strike-slip movement at transcurrent faults. U.T.M. 33S map projection. (For interpretation of the references to colour in this figure legend, the reader is referred to the web version of this article.)

naturally generated by consequent combined gravity spreading and sliding. Using this series of laboratory analogue models, we successfully simulate all the major fault systems of Etna. We demonstrate why they are there, and how they interact with each other. This provides a structural system on which to place observations of deformation, and to frame eruption, landsliding and seismic hazards.

2. The fault systems of Etna

There are several major zones of faulting on Etna, illustrated in the map of Fig. 1. Either side of the summit are the north-south bounding faults of the cryptic summit graben. On the flanks, in clockwise order from the north, there are the Pernicana fault system, an arcuate left-lateral strike-slip fault running from the Northeast Rift, curving round towards the east, and then ESE towards the Ionian sea. Southeast of the Pernicana fault is the Ripa della Naca, a prominent step fault system running northeast from Citelli, downthrown towards the southeast. Running down the east flank of Etna is a series of normal faults trending about N10°W to N-S, known as the Timpe system. At their south end one of them becomes the Acireale fault, a prominent coastal fault downthrown eastward into the Ionian sea. South of Etna are three prominent right-lateral strike-slip fault systems, the Trecastagni fault, the Mascalucia-Tremestieri fault, and the Gravina fault, the most southerly fault on Etna. On a similar alignment are the Tarderia faults, briefly exposed nearer the summit cone. Finally, much further west are the north-south right-lateral strike-slip Ragalna faults.

2.1. Summit Graben

The most active Etna faults, at least in terms of their cumulative movement, are those bounding the cryptic summit graben (Murray, 2019). Mean annual rates of graben subsidence 1975–2018 vary from 88 mm y^{-1} north of the summit to 61 mm y^{-1} south of it. Extension across the graben is even greater, at 229 mm y^{-1} (north) to 179 mm y^{-1} (south of summit). Episodes of graben sinking and widening have been contemporary with flank eruptions, notably 1981, 1983, 1985, 1989, 1991–3, 2002–3, 2008–9, 2014 (Gambino et al., 2016) and 2018 (Pezzo et al., 2020). In each case, sinking and extension accelerates rapidly at the start of the eruption, and then returns to slower rates over 1 to 3 years. This extension is magma-assisted as opening dykes force the rocks apart, creating slivers of uplift close to the dyke in a few cases. The greatest and most widespread sinking and extension occurred during the north-south bilateral eruption of 2002–2003, when most measuring stations both north and south of the summit were affected.

2.2. The Pernicana fault

This is the most active of the Etna flank faults. It originates at the Northeast Rift, whose eastern side is the site of a listric fault (well seen in the Piano Provenzana) kinematically connected to the Pernicana fault (Groppelli and Tibaldi, 1999). Near its proximal end, movements are clearly visible where the fault crosses roads. Serious cracking has been caused during local earthquakes on at least twelve occasions 1980–2020 south of Mareneve (Obrizzo et al., 2001; Bonaccorso et al., 2013) and smaller seismic events occur with monthly frequency (Lo Giudice and Rasà, 1992). The southerly dip-slip component of this fault has been documented meticulously by repeated occupations of a precise levelling traverse installed in 1980 (Obrizzo et al., 2001). These show a total of 940 mm subsidence 1980–2019 of the southern side of the fault at this location, or a mean annual drop of 24 mm y^{-1} (Murray, 2019). The left-lateral strike-slip component is of a similar order, averaging about 26 mm y^{-1} (Neri et al., 2004), though this can briefly accelerate up to 100 mm y^{-1} following eruptions (Bonaccorso et al., 2006; Bonforte et al., 2008). Lower down the fault near Vena, precise geodetic and GPS measurements between 1997 and 2005 gave mean strike-slip values of 28 mm y^{-1} (Palano et al., 2006; Bonforte et al., 2007). More recently, a total of 7 slow-slip events occurred between 2009 and 2015 when a continuous GPS network either side of the fault was installed specifically to measure such events, resulting in a mean slip rate of 26 mm y^{-1} (Palano, 2016). The fault can be traced as far as the sea, in the displacement it has caused to walls, buildings and road edges (Tibaldi and Gropelli, 2002). The left-lateral movement remains about the same all along the fault, though sticking in some places more than others. Near the sea at Gona it has moved 1370 mm in about 70 years, or 20 mm y^{-1} (Neri et al., 2004), and Garduño et al. (1997) find values of 26 ± 5 mm y^{-1} since 1874. It has been continuing at these rates throughout the Holocene: matching up points on a cinder cone near Mareneve dated at 13,700 years B.P., Tibaldi and Gropelli (2002) derive a strike-slip displacement of 370 m, giving a mean value of 27 ± 7 mm y^{-1}, corresponding to the background rate of 26 mm y^{-1} (Palano, 2016) within the stated error.

2.3. The Ripa della Naca and nearby faults of similar orientation

Marked by a prominent southeast-facing fault scarp over 100 m high, the Ripa della Naca has been inactive for the past 15,000 years (Tibaldi and Gropelli, 2002). Nevertheless, the Ripa della Naca faults played a critical part in the 1928 eruption, creating a preferential pathway for magma that erupted above the town of Mascali, completely destroying it in less than a week (Branca et al., 2017).

In a similar orientation, but 5 km east, lies the Piedimonte fault, also downthrown southeastward. This fault is active, with vertical slip rates of 1 to 2 mm y^{-1} throughout the past 500 kyr, (Monaco et al., 1997; Tibaldi and Gropelli, 2002), and it cuts across the Pernicana fault. The Carruba faults also share the same orientation, but are 12 km southeast of the Ripa della Naca, by the sea.

2.4. The Timpe fault systems

"Timpe" (singular: "timpa"), is a local name for the prominent seaward-facing fault scarps down the lower east flanks of Etna. They are oriented between north-south and northwest-southeast, and whilst most are normal faults downfaulted towards the east, there are also some downthrown west, including the San Alfio fault (Fig. 1), the most northerly, which has had vertical slip velocities 1 to 2 mm y^{-1} over the past 80,000 years (Monaco et al., 1997), and extension a fraction of this. In places the westward and eastward-facing faults form graben and horsts. They include the parallel Trepunti and Leonardello faults which together form a 5 km graben. The most westerly Timpe fault, the Linera fault, is oriented N 40° W, and has a slight right-lateral component of movement. At its southern end it runs into the Acireale fault, which forms a prominent north-south cliff 50–100 m high for 7 km down the coastline. Most of these faults are associated with shallow seismicity, and have had vertical slip rates of between 1 and 2 mm y^{-1} over the past 1 to 168 kyr (Monaco et al., 1997). Like the Pernicana fault, much higher rates are possible over short time periods: Azzaro et al. (2020) recorded over 100 mm of vertical displacement at the San Leonardello fault associated with seismic and creep events in 2009 and 2016. The Timpe fault system probably relates to the instability of the submarine margin (e.g. Argnani et al., 2013; Chiocci et al., 2011; Gross et al., 2016, Azzaro et al., 2020).

2.5. The Mascalucia-Tremestieri, Trecastagni & Gravina fault systems

There are at least three transcurrent faults, all with right-lateral slip, that make up a southern boundary to the sector of eastward movement of the east flank of Etna. In this way they correspond to the Pernicana fault in the north, though since the strain release is taken up by 3 faults, they are individually less active than the Pernicana fault, with smaller annual rates of displacement. The Mascalucia-Tremestieri fault is at least 12 km long, and has a similar radius of curvature to the Pernicana fault, though curving northwards rather than southward. Gross et al. (2016),

using High resolution 2D seismic data, demonstrate that a prolongation of this fault extends a further 12 km eastward beyond the shoreline. The Gravina fault is the most southerly of the Etna faults, lying parallel to the Mascalucia-Tremestieri fault but about 3 km south of it.

The Fiandaca-Pennisi faults, which form part of the Timpe system in its northern part, intertwine with the Nizzeti fault at its southern end. A large earthquake (Mw 4.9, epicentre 0.4–1 km depth) occurred at the northern part of the Fiandaca-Pennisi fault on 18th December 2018, causing severe damage to nearby towns and villages (Civico et al., 2019). The event reactivated faulting for 8 km along strike, with a strike-slip component of displacement attaining 350 mm in places, though the average value is 90 mm (Villano et al., 2020). The Nizzeti fault joins the Mascalucia-Tremestieri fault close to the Ionian shore, curving round southeastwards as it does so. The Trecastagni fault is also similar to the Timpe system in orientation, running about N 20° W, but has a right-lateral motion, and runs into the Mascalucia-Tremestieri fault at its southern end. Its northwestern end possibly continues into the western Tarderia fault, and perhaps even further into the right-lateral strike-slip dry fissure on the outer southern slope of the Valle del Bove that accompanied the start of the 1989 eruption (Ferruci et al., 1993). The central and eastern Tarderia faults may perhaps connect with other faults in the outer southern Valle del Bove wall, and may extend further south into the area between the Fiandaca-Pennisi Faults and Trecastagni faults, but possible exposures are covered by the 1792–3 and 1634–6 flows in the north, and by flows of medieval age to the south.

The creep of this system of southern faults was followed seismically in the 1980s by Lo Giudice and Rasà (1992) and in the 1990s using radar interferometry by Froger et al. (2001) and Ranvier (2004), also by Urlaub et al. (2018) in 2016–2017. Phases of creep and seismicity lasting up to 16 months were observed. The radar interferograms show clearly that both the Mascalucia-Tremestieri and Gravina Faults extend further northwest than was previously suspected from geological exposures, the former connecting to the southern rift zone of the volcano, strengthening its correspondence to the Pernicana fault in the north. Velocities of right-lateral creep 1993–1997 were of the order of 15 mm y^{-1} for the Gravina fault, 10 mm y^{-1} for the Mascalucia-Tremestieri fault, and 5 mm y^{-1} for the Trecastagni fault (read from Ranvier, 2004 interferogram map). Similar values were found by Solaro et al. (2010), and Bonforte et al. (2011), analysing a range of interferograms 1995–2000, derived annual right-lateral displacements of 5 mm y^{-1} for the Gravina fault, and 15 mm y^{-1} for the Mascalucia-Tremestieri fault, at a time when the Pernicana fault showed stronger left lateral displacement of 25 mm y^{-1}. As with other faults, much higher rates are possible during single events: in May 2017, 40 mm right-lateral slip in 8 days was measured across the seaward extension of the Mascalucia-Tremestieri fault (Urlaub et al., 2018). Similar slow-slip events had earlier been observed onshore at the lower eastern flank (Bruno et al., 2017).

2.6. Ragalna faults

These are the furthest southeast of any of the active Etna fault systems. The main faults are downthrown on the east side, with long term dip-slip movement of up to 1.4 mm y^{-1}, and are the site of periodic earthquakes and aftershocks, as in 1977–78 (Cristofolini et al., 1981), and 1991 (Ferruci and Patané, 1993). Both these events gave fault-plane solutions revealing right-lateral displacement.

Rust and Neri (1996) and Neri et al. (2007) argue that the Ragalna faults mark the western boundary of the unstable eastern sector of the volcano, corresponding to the Pernicana fault system in the northeast. If this is the case, it places the western boundary 12 km further west than the Mascalucia-Tremestieri/Gravina fault systems favoured by previous workers.

2.7. Cryptic Western graben

In addition to the known and described faults above, there is a pronounced area of subsidence west of the summit cone between Monte Palestra and Monte Pecoraro, shown in Fig. 1, which we have designated the Western graben, and are describing here for the first time. It has subsided steadily since this precise levelling traverse was first occupied in 1980, attaining a maximum subsidence of 491 mm at the levelling benchmark 1 km north of Monte Palestra by 2018, i.e. at a mean subsidence rate of 12.9 mm y^{-1}. The southern and western limits are clear from the levelling data, but northern limits of the subsidence are poorly defined due the paucity of stations. However, a GPS station west of Monte Guardirazzi lies more or less in the centre of the northward projection of the graben, and has subsided 83 mm in the ten years 2008–2018, i.e. a not too dissimilar rate of 8.3 mm y^{-1}. Both these subsidence values are compared to the reference zero of a station north of Monte Maletto. Regarding lateral extension across the area of subsidence, the record of deformation is also only a decade, but GPS stations at Monte Palestra and Monte Pecoraro moved apart 39 mm between 2008 and 2018, i.e. an extension rate 3.9 mm y^{-1}, less than half the rate of subsidence, though the time period may not be representative of the longer term.

No traces of any surface faulting have yet been found in association with this feature, but the area is far from any paths and is well vegetated, and there are several recent lavas flows from the 18th century to the present which have covered parts of it. It is similar to the summit graben in these respects, but the rates of subsidence are an order of magnitude less, and unlike the summit, the rate of lateral extension is less than the rate of subsidence, no doubt due to the fact that extension is not magma assisted here. Bousquet and Lanzafame (2004) show extension lower down the western flank, near Bronte.

3. Laboratory analogue modelling

We have created analogue models of the fault systems described above in the laboratory, following the same methodology as the experiments originally carried out by Merle and Borgia (1996) which have now become standard practice in studies of this kind (Merle and Lénat, 2003; Wooller et al., 2004). In most previous studies, the approach has been to make models of general cases. The approach differs here, in that we aim to model a specific case, by scaling the main material properties and topographic features of Etna, and then observing the resulting structures produced and their evolution. Our model setup, designed to achieve this specific case is shown in Figs. 3 and 4.

3.1. Model configurations

Mt. Etna is built on a sedimentary basement, with an overall slope of about 2° to the ESE (Fig. 2). To the northwest, the basement consists of a 17 × 7 km plateau that is almost horizontal, and underlies most of this quarter of the volcano (Branca and Ferrara, 2013). 1 km northwest of the summit, the basement starts to steepen, and the east side of the volcano slopes continuously towards the sea, with at least two broad valleys also running seaward. The Etna volcano itself comprises a steep sided summit cone built up by repeated eruptions at or near the summit, and a much broader apron of lavas fed by flank eruptions lower down the volcano (Fig. 2). The apron of lavas is about 500 m in depth, but attains 900 m nearer the foot of the summit cone, thinning to 200 m or less in upslope distal regions.

Our models follow in each case the nature of Etna and its substrata and the layout of Fig. 2, with small variations in shape and proportions to gauge how this affects fault configurations. The sub-volcanic sedimentary basement on which Etna lies is represented by a layer of silicone putty (this is the same silicone as used in other such experiments, such as Merle and Borgia, 1996, Wooller et al., 2004, Delcamp et al., 2011) . This is a ductile material that slowly flows until its surface becomes level, which happens after about 12 h under ambient conditions. The particular silicone putty used has a characteristic viscosity of about 20,000 Pa.s, as tested with the laboratory viscometer, and contains small

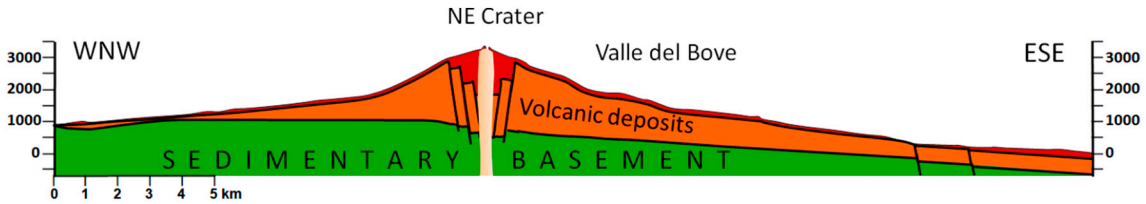

Fig. 2. Schematic geological cross-section of Mt. Etna, simplified after Branca and Ferrara (2013). The mainly Quaternary sedimentary basement is shown in green, older volcanic deposits in orange, and recent lavas in red. (For interpretation of the references to colour in this figure legend, the reader is referred to the web version of this article.)

amounts of sand, raising its viscosity slightly. This does not affect geometric results, but slows model deformation rates slightly. The putty is placed on a flat board on a bench, and left to find its own level. To stop the putty flowing off the board, in most experiments a rampart of sand is placed all around the edges, which in some places will later also represent the mountains around Etna. The model is then left overnight, by which time the silicone putty has formed a lake surrounded by sand ramparts, as in Fig. 3A. Next, a layer of sand is placed over the putty layer. Its surface is levelled by dragging a long straight edge across the top of the sand layer, the straight edge being supported by horizontal guides either side of the model to keep it level. This layer of sand, which behaves as a brittle material, represents the extensive apron of lavas that surround the summit cone of Etna below about 2000 m. The sand is a quartz sand from Nemours in France, and has an average grain size of 300 μm. It is used with about 5% plaster, the plaster giving the mixture cohesion (50 Pa), to fit the scaling with brittle rocks. The cohesion allows surface cracks to form, and so faulting is clearly expressed. This procedure is the same as used in Delcamp et al. (2011), Wooller et al. (2004), and other studies reviewed in Galland et al. (2015) and Merle (2015).

The summit of Etna is represented by a sand cone, placed off-centre to the north as on Etna, and the entire model is sprinkled with plaster powder, and dusted with pepper to provide identifiable reference points for measurement. The model is then tilted slightly to the right, to represent the sloping basement of Etna, and the sand at the bottom of the slope removed, to represent the unbuttressed seaward side of Etna (Fig. 3D). Some surrounding sand is also removed from the top right edge, corresponding to where the Peloritan Mountains end, and in some experiments along the bottom right edge, to represent the end of the low range of hills south of Etna (Fig. 3C).

The model starts to visibly deform and change shape after a few minutes, and surface cracks appear after 15 to 20 min. These develop into faults and graben which become more pronounced and numerous as the experiment progresses. The experiment is usually stopped after an hour or so, though occasionally it is left to run for two or three hours.

3.2. Scaling analysis

The parameters used in the scaling analysis are illustrated in Fig. 3. The relative dimensions and position of the cone, thickness of the sand and silicone putty layers etc. are chosen to match those of Etna, and varied in the different models where a range of values exist, or if values

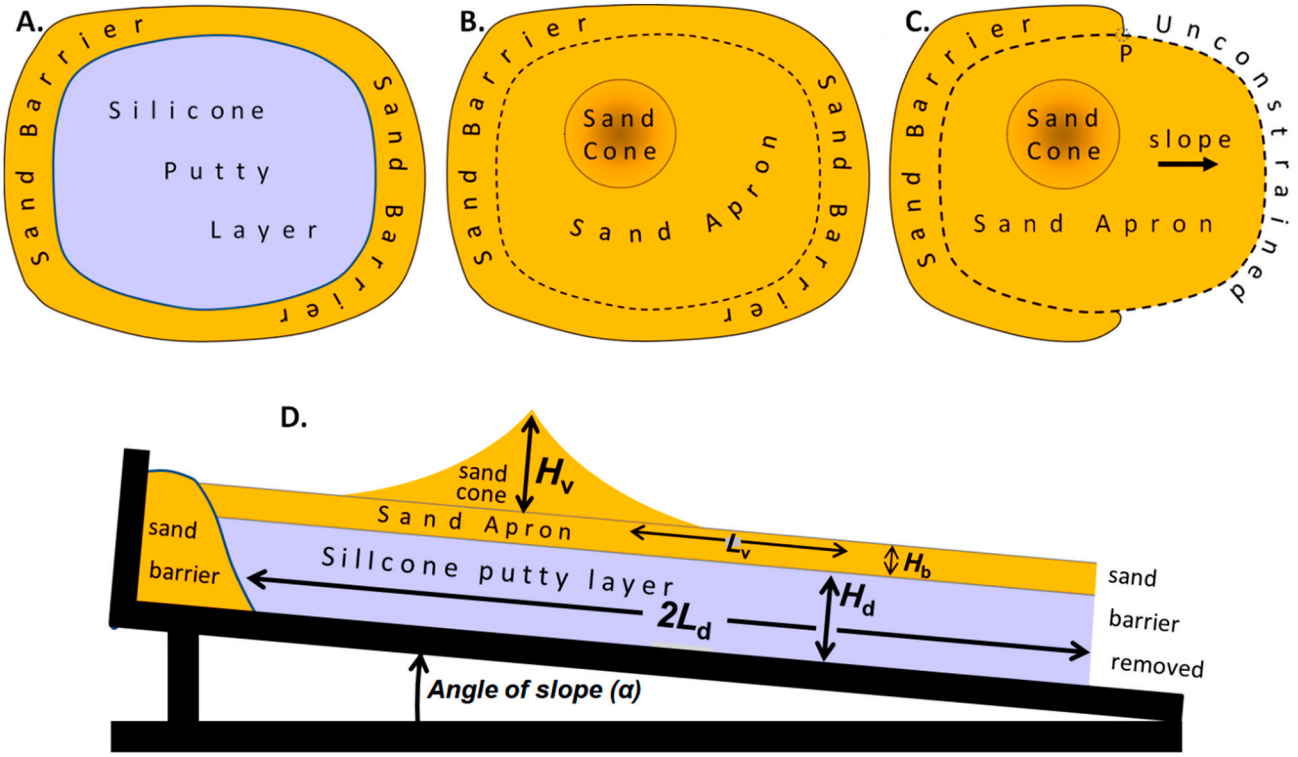

Fig. 3. Top: Plan view of the experiment assembly and setup for the analogue modelling: A. Silicone putty layer emplaced over base board, surrounded by sand barriers. B. Sand apron in place over silicone putty layer, with sand cone on top. C. Base board tilted to right, downslope sand barrier removed to create the unconstrained edge, experiment begins. **Bottom:** (D) Cross section of the experimental setup for the analogue modelling at the start of the experiment. Dimensions and material properties are matched to those of Etna. See text and Tables I and II for details.

are only known within given limits. Table 1 gives a list of geometric variables and material properties for the principal parameters of Etna, as far as these are known, and the model. The scaling method of Merle and Borgia (1996) is used, but with an extra term for substratum slope introduced by Wooller et al. (2004), and for the introduction of cohesion in the sand layer (Delcamp et al., 2011).

The laboratory variables scale up to those on Mt. Etna within the uncertainty of the latter values. For each variable, or parameter, a rounded up reference value is chosen for the scaling ratio. These are then used to calculate the time and velocity scaling, as given in Table 1. Etna values for H_b and H_d are derived from Branca and Ferrara (2013); other properties from Wooller et al. (2004), Merle and Borgia (1996), Delcamp et al. (2011), Galland et al. (2015), and Merle (2015).

The stress ratio is calculated from the length scale, gravity scale and density scale (p.g.h $= \sigma$, stress), and allows the cohesion scale to be known, as this is the same as the stress ratio. Time ratio is calculated from the ratio of viscosity to stress (μ / σ), and velocity from the length scale divided by the time scale. The velocity scale allows the rate of fault movement on Etna to be compared with the model rates. The viscosity of the substrata and the cohesion of the rocks are difficult to estimate in nature (Delcamp et al., 2011; Galland et al., 2015), so the velocity rate will only be approximate in the models. But the range of different fault movements in the models is consistent with the range seen on Etna. In the analysis below, displacement rates of Etna faults are compared with their model rates and used to check the scaling ratio, which is the same order of magnitude.

3.3. Laboratory experiments

Altogether, 14 laboratory experiments were carried out, each one using slightly different values for the thickness of the layers of sand and silicone putty, the summit cone height and shape, the slope angle of the basement, the angle of the spreading sector, and the position of the summit cone. Ten of these gave end results similar to the real situation on Etna. The top part of Table 2 shows details of each of the selected experiments.

The sand layer and the silicone putty layer are varied in thickness, because the apron of lavas and the layer of ductile sediments beneath Etna also vary in thickness (Branca and Ferrara, 2013); Fig. 2. Different values for the summit cone height and base width reflect the varying height of Etna's summit over the past 300 years, and the north-south elongation of Etna's summit cone. The slope of the basement also varies from around 0° beneath the northwest flank to 4° in parts of the eastern flanks. The time for Etna to deform is fixed at 10^{12} s, i.e. just over 30,000 years. This is a time period long enough for all major structures to form at the observed natural displacement rates, and is a time period over which Etna has largely maintained its present position and shape (Branca et al., 2011b; De Beni et al., 2011).

The sand cone was circular in most experiments, as this was easiest to standardise by pouring sand through a funnel, but in 3 experiments the cone was roughly elongated (e.g. Fig. 4). The placement of the cone on the sand layer was critical to the formation of some of the fracture fields, and is listed in Table 2 as N-S eccentricity and E-W eccentricity. A range of values was tried in each case.

4. Results

Table 2 (bottom) shows the results of each experiment. Ticks indicate the fault system is present in the experiment. A question mark is given if the faults had an orientation differing by more than 10°, or were weak or more pronounced or more extensive than on Etna. All the faults named in Fig. 1 appeared in at least 4 of the 14 simulations, and faults corresponding to the summit graben, Pernicana fault, Ripa della Naca, Tarderia faults and the Ragalna fault were present in 11 or more of the 14 simulations. The width of the summit graben in each model is given at the top, as a fraction of the summit cone width. Fig. 4 illustrates experiment 11, both at the start, and after running for 50 min, when many analogues of the above faults are visible. It should be noted that the faults ticked in Table 2 were not necessarily visible at every stage of the experiment: some changed character or were obscured by later fault development. Fig. 7 (middle row) shows experiment 7 after 43 min, and also after 237 min. New faults have appeared, straight faults have become curved, and fault movement has increased at some faults, and decreased at others.

4.1. Model to Etna fault correspondence

We now examine each of the fault systems appearing in the models, and how these correspond to what actually happens on Etna. For convenience, the direction of downwards slope towards the right edge of each model is referred to as east, and the other edges accordingly, even though the direction of basement slope on Etna is closer to east-southeast. Fig. 5 illustrates one of the successful models, experiment 8, after 87 min. Comparison with Fig. 1 will show that clear analogues of most of the fault systems have formed. North-South summit graben are the most pronounced features, together with many fractures in similar positions and orientations to historical eruptive fissures. Northeast of the fractured sand cone, left-lateral transcurrent faults corresponding to the Pernicana fault are visible, and to the east extensional faults resembling the Timpe faults, and to the south, a series of right-lateral

Table 1
Scaling parameters: Values for the geometric variables and material properties (defined below in Section 3.2) in nature and the analogue laboratory experiments.

	Variable	Units	Etna	Laboratory	Scaling Ratio
H_v	sand cone height	m	1100–1600	0.027–0.060	4×10^{-5}
L_v	sand cone radius	m	3200–6000	0.046–0.089	4×10^{-5}
H_b	sand apron thickness	m	200–900	0.01–0.02	4×10^{-5}
H_d	thickness of silicone putty layer	m	>89	0.009–0.025	4×10^{-5}
L_d	radius of silicone putty layer	m	>32,000	0.11–0.27	4×10^{-5}
α	angle of substrate dip	degrees	0°–4°	0° - 2°.7	1
ρ_v	sand cone density	kg m^{-3}	2500	1400	0.5
ρ_b	sand layer density	kg m^{-3}	2500	1400	0.5
ρ_d	silicone putty layer density	kg m^{-3}	1900	1000	0.5
Φ	sand angle of internal friction	Pa	35°	35°	1
σ	cohesion of brittle material	Pa	10^7	50	5×10^{-5}
μ_d	ductile layer viscosity	Pa.s	10^{19}	2×10^5	2×10^{-14}
g	force of gravity	m s^{-2}	9.81	9.81	1
T	time span of deformation	s	30,000 yr	2.1×10^3–11.76×10^3	4×10^{-8}
t	time scale from μ_d / σ	s	10^{12}	10^4	10^{-8}
u	Velocity (length scale/time scale)	m s^{-1}	1 cm yr^{-1}	0.01 m hr^{-1}	1×10^4

Table 2
(Top) Values for the geometric variables in 10 analogue laboratory experiments, plus notes on boundary conditions. **(Bottom)** Results of the 10 experiments. A tick (√) indicates that a feature resembling the fault is present in the model, a query (?) means that a similar feature is present but slightly different from the fault on Etna. Numbers of fault systems definitely present in each model are given at the bottom, and as a percentage of all the Etna fault systems named in Fig. 1. Numbers of experiments which contained each of the Etna fault systems are given in the columns to the right, with percentages of the total number of experiments also.

Experiment No:	***2***	***6***	***7***	***8***	***9***	***10***	***11***	***12***	***13***	***14***			***MEANS***
Duration (minutes)	57	121	196	111	79	75	51	60	65	35			***91 min***
Silicon putty thickness mm	21.5	21	14	11	9	9	14	12	16	21			***16 mm***
Sand apron thickness mm	20	20	10	10	15	11–5.	20–8.	20–8.	20–0.	20			***14 mm***
Cone height mm	45	45	60	45	45	45	45	45	45	45			***41 mm***
Cone base width mm	95	161	170	150	159	162	178	150	140	154			***136mm***
Flared cone?	yes	yes	yes	yes	yes	yes	yes	yes	yes	yes			
Elongate cone?	no	no	no	no	no	yes	yes	no	no	yes			
Basement slope	(4°)	2°	2°	2°	2°	2°.7	2°	2°	2°	2°.6			***1°.9***
N-S eccentricity. Central = 0	39	39	25	30	22	23	47	24	42	24			***27***
E-W eccentricity. Edge = 100	22	47	33	35	30	33	54	60	39	4			***28***
Basement N-S mm	613	260	480	370	460	470	340	380	380	280			***374 mm***
Basement E-W mm	380	300	480	400	540	540	390	450	330	220			***381 mm***
Notes	slope in one step		Base is 7 mm E - W valley	slope steepens to east		sand layer thins to E	sand layer thins to E	sand layer thins to SE	sand layer thins to SE	Valle del Bove scooped out after 30 m			
ETNA FAULTS REPRESENTED IN THE ABOVE MODELS:											***TOTALS***	***%***	
Summit graben width:	0.30	0.28	0.30	0.24	0.28	0.20	0.28, 0.34 (2 graben)	0.38	0.30	0.22			***0.28***
Summit graben	√	√	√	√	√	√	√	√	√	√	**12**	**86%**	Summit graben
Pernicana fault	?	√	√	√	√	√	√	√	√	√	**11**	**79%**	Pernicana fault
Piedimonte fault		√			√		√		√	√	**5**	**36%**	Piedimonte fault
Ripa della Naca	√	√	√	√	√	√	√	√	√	√	**12**	**86%**	Ripa della Naca
Trepunti fault	√	√	√	√					?	√	**7**	**50%**	Trepunti fault
Leonardello fault	√	√	√	√					?	√	**7**	**50%**	Leonardello fault
Acireale fault	?	√	√	√			?	?	√		**4**	**29%**	Acireale fault
Nizzeti faults		?	√	√					?		**3**	**21%**	Nizzeti faults
Trecastagni fault		√	√	√	√		√		√		**8**	**57%**	Trecastagni fault
Mascalucia-Tremestieri fault		√	√	√	√		√				**7**	**50%**	Mascalucia-Tremestieri
Tarderia fault	√	√	√	√	√	√	√	√	√	√	**13**	**93%**	Tarderia fault
Ragalna fault system	√	√	√	√	√		√		√	√	**11**	**79%**	Ragalna fault system
Carruba faults			√	?			√	√		√	**6**	**43%**	Carruba faults
San Alfio fault	√	√	√	√					√	?	**9**	**64%**	San Alfio fault
Linera fault		√	√		√				√	√	**6**	**43%**	Linera fault
Gravina fault			√	√			√				**4**	**29%**	Gravina fault
TOTALS (certain):	**7**	**13**	**15**	**13**	**9**	**4**	**10**	**5**	**10**	**10**			
% Etna faults in model:	44%	81%	94%	81%	56%	25%	63%	31%	63%	63%		**56%**	

Fig. 4. Experiment No. 11 (left) at the start, and (right) after running for 50 min. Slope of the base is 2° to the right. In this experiment, an attempt has been made to represent the north-south elongation of the summit cone of Etna, with the Northeast Rift. The dashed line down the right side of the left image shows where the sand barrier has just been removed, creating an unconstrained lower edge. After 50 min (right), the underlying ductile silicone putty has spread towards the unconstrained sector (arrows), carrying the right side of the sand cone and apron with it, creating a north-south summit graben and fault patterns similar to those of Etna. Black scale bar (lower left) is 5 cm long.

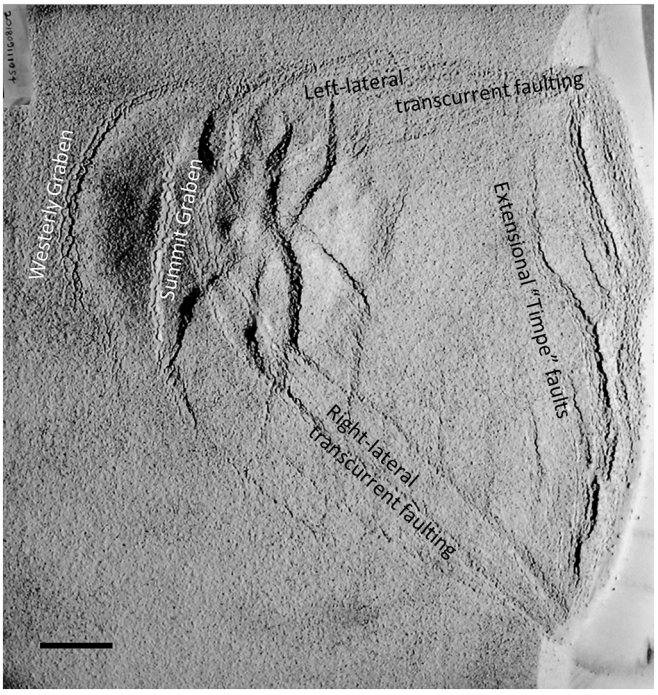

Fig. 5. Experiment 8 after 87 min, scale bar (lower left) is 5 cm. The sand cone is bisected by north-south graben, connecting to left-lateral faulting (top right) resembling the summit graben, northeast rift and Pernicana fault system on Etna (see Fig. 1). At the right edge, north-south fracturing similar in position and configuration to the Timpe faults is visible, and to the south, converging curved right-lateral faults similar to the Tremestieri, Mascalucia and Gravina faults can be seen. The curved extensional fault around the western foot of the summit cone corresponds to an area of east-west extension and subsidence revealed from geodetic and GPS measurements from 1980 onwards, and here named the Western Graben. See text for details.

transcurrent faults similar to those in Fig. 1.

4.1.1. *Summit graben*

Figs. 4, 5, 6 & 7 show a well-defined north-south summit graben in every experiment. This is usually the first feature to develop, and becomes wider and more pronounced as the experiment progresses. These graben are the result of two processes operating in every model. The stresses within a gravitationally spreading sand cone inevitably result in the formation of leaf graben (Merle and Borgia, 1996). At the same time, downslope sliding increases tensional stress in the east-west direction, thus augmenting the formation of leaf graben oriented north-south, but suppressing those oriented east-west. There is an interplay between these two processes, so if gravitational spreading dominates then leaf graben can form in other directions than north-south. In experiments 12 and 13 (Figs. 6 bottom right and 7 top left), an attempt was made to represent the thinning of the lava apron towards the sea by thinning the sand apron from 20 mm beneath the sand cone to 8 mm and 0 mm respectively at the eastern unconstrained edge. This differential load on the silicone putty beneath the cone has meant that spreading of the cone is relatively greater in these models, producing leaf graben oriented 10° to 30° from the north-south graben (model 12), and at around 50°, 120° and 150° in model 13. Some of the bounding faults of these graben are at similar positions and orientations to fractures formed during the 1983, 1985, 1989, 1991–3 and 2001 flank eruptions.

4.1.2. *Pernicana fault system*

A fault starting at the northern end of the summit graben is present in most models, usually departing northeastwards and curving round to the east. This fault marks the boundary between restraining stresses caused by the topography to the north and the unrestrained eastern sector. Gravitational spreading of the sand cone northwards is obstructed by the presence of the sand ramparts representing the Peloritani mountains. This obstruction creates a relatively stable area to the left of point P in Fig. 3C. However, to the right of point P there is no such obstruction, so the cone can continue to spread freely in this direction. The dichotomy between these conflicting stresses is resolved in the formation of a left-

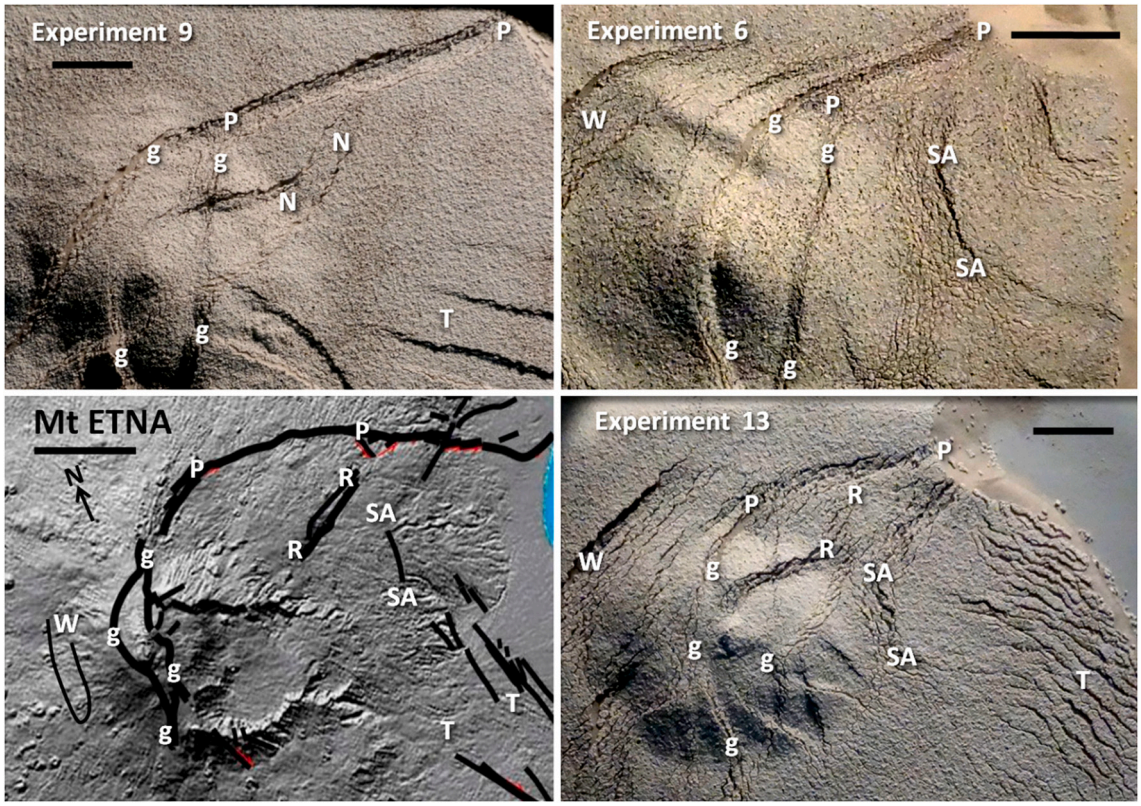

Fig. 6. Regions to the northeast of the sand cone in three experiments, with lighting from the east or northeast, together with a map of faults in the equivalent region of Mt. Etna (lower left), rotated so that the downslope direction matches that of the models. The Pernicana fault is marked P P, the Ripa della Naca N N (Experiment 9), or R R (Experiment 13), the San Alfio fault SA SA, Timpe faults T, summit graben bounding faults g g, and analogues of these faults in the various experiments are similarly labelled. Curved east-west extensional features marked W correspond to the Western Graben (Fig. 1). The black scale bar is 5 km on Etna, and 5 cm in the experiments. See text for details.

lateral strike-slip fault, corresponding to the Pernicana fault.

Fig. 6 shows the regions north of the sand cone in three of the experiments listed in Table 2. Analogues of the Pernicana fault, marked P at each end, are visible in all of them. In each case at the lower left end they merge into the summit graben bounding faults (marked g) and terminate distally at the top edge of the model at the point where the sand rampart obstructing the putty has been removed. Experiment 9 has a single well-defined straight fault, whereas experiment 13 has a curving broad area of en échelon fissuring indicating left-lateral movement, and a parallel fault system at the northwest foot of the sand cone. Experiments 6 and 13 have additional parallel faults, some of them close to the eruptive fissure positions of 1947 and 2002.

4.1.3. Ripa della Naca and San Alfio faults

Faults resembling the Ripa della Naca are seen in models 9 and 13 (Fig. 6), though in both cases they are small compared to the prominent fault scarp on Etna. They appear to have formed in response to the accumulating tensional stress as the silicone putty spreads downslope. West dipping faults aligned north-south appear further east in experiments 6 and 13 marked SA in Fig. 6. They appear to be transpressional, at least in experiment 6, and are close to the San Alfio fault in position, orientation and dip direction. They lie at the downslope foot of the sand cone, where slope-assisted gravitational spreading comes against the slower-moving sand apron.

4.1.4. Timpe faults

In most experiments, as soon as the sand barrier is removed from the downslope edge of the model and the silicone putty starts to flow and spread out down this unconstrained slope, northwest-southeast tensional cracks start to appear at the east edge in similar orientation and position to Timpe faults such as Trepunti, Leonardello and Linera, although these model faults are much more numerous in most experiments than on Etna. They are marked T in Fig. 6, experiments 9 and 13. The orientation of the model Timpe faults further west seem to be particularly sensitive to small relative changes in tensional stresses caused by downslope flow of the silicone putty, and those caused by spreading following the removal of sand from the northeast and southeast edges. For example, in some models where longer sections of the north and south sand barriers are removed, almost east-west cracks and graben develop (marked T in experiment 9, Fig. 6).

North-south faults corresponding to the Acireale fault have developed at the lower right edge of experiments in Fig. 7, where they are marked A. As on Etna, these model faults show a primarily extensional motion, without a strike-slip component in most cases.

4.1.5. Mascalucia-Tremestieri, Trecastagni & Gravina fault systems

Curved faults of similar orientation are found in the same position as the Mascalucia-Tremestieri fault in about half of the experiments in Table 2; the appearance of these model faults can be seen, marked M, in the simulations of Fig. 7. In each case they extend much further towards the cone than the surface exposures on Etna, joining the bounding faults of the summit graben. This corresponds to the similar northward extension of the Mascalucia-Tremestieri fault as far as the southern rift visible in radar interferograms (Froger et al., 2001; Ranvier, 2004; Bonforte et al., 2011). A feature marked Tr corresponding to the straighter Trecastagni fault is also visible to the north, that joins the Mascalucia-Tremestieri fault analogue close to the bottom right corner of the models, this junction being rather further east than the real Trecastagni fault. In most models a fainter and more discontinuous curved fault G southeast of the Mascalucia-Tremestieri fault analogue and

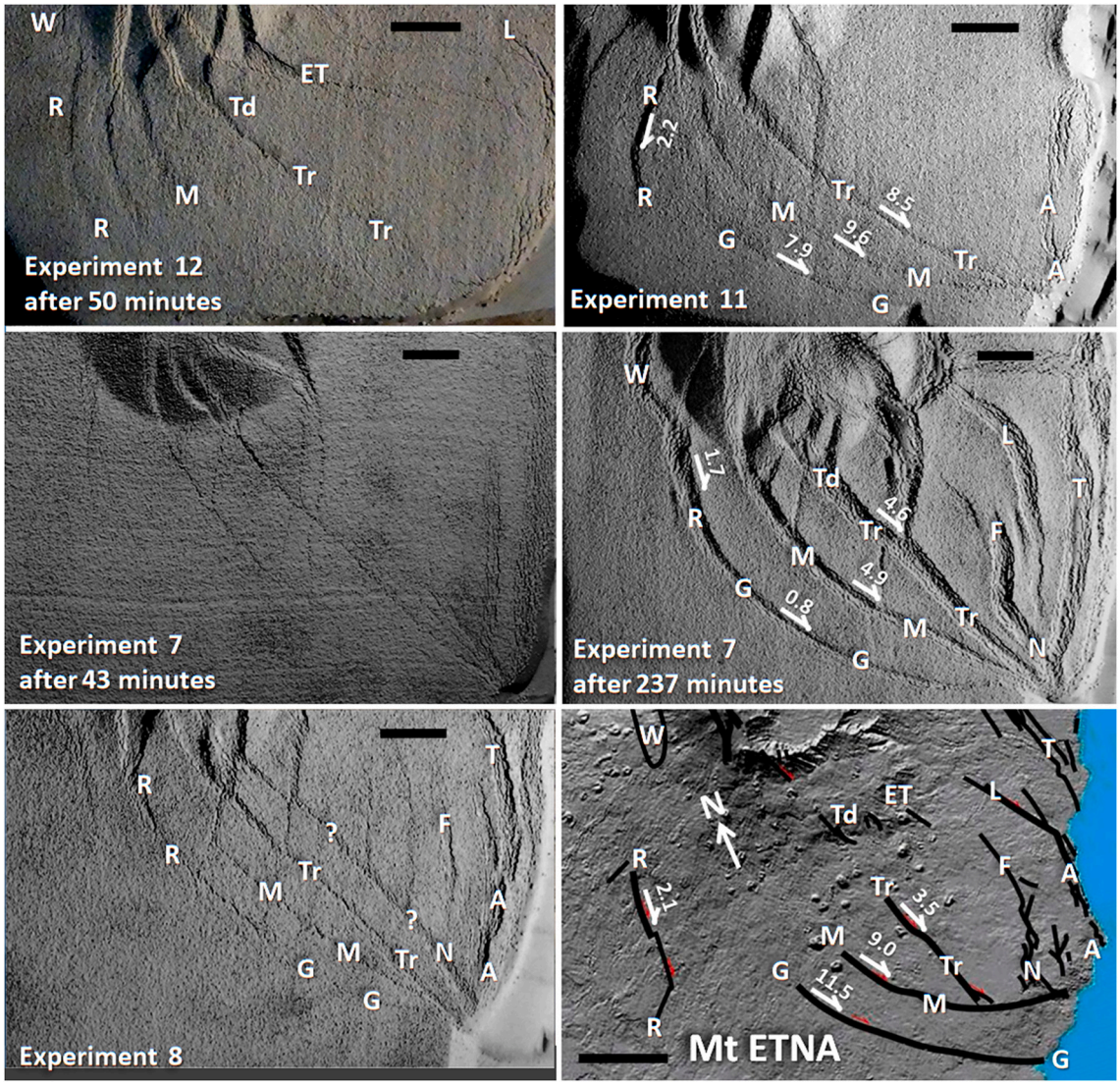

Fig. 7. Fault formation in the southeastern sector of four of the experiments listed in Table 2, plus a map of faults on Mt. Etna in the equivalent location (bottom right), rotated so that the downslope direction matches that of the experiments. Basement slope of the models is 2° to the right (east), and lighting from the east or north. Prominent strike-slip faults are marked with their slip direction and annual rate of slip in mm y^{-1}, having been scaled as described in the text. Field measurements of strike-slip rates at the equivalent Etna faults are shown in the map bottom right. Experiment 7 is shown at two stages 194 min apart, and many changes in fault configurations are visible. Faults south of the sand cone have become more curved, and right-lateral strike-slip movement is evident in many places. New tensional faults have also appeared southeast of the sand cone. As in Fig. 6, the faults are labelled with their Etna equivalents, A A referring to the Acireale fault, ET to the eastern Tarderia fault, G G to the Gravina fault, L to the Linera fault, M M the Mascalucia-Tremestieri fault, N the Nizzeti fault, R R the Ragalna fault, F the Fiandaca-Pennisi Faults, T to the Timpe faults, Td to the two western Tarderia faults, Tr to the Trecastagni fault, and W to the Western Graben. The black scale bars are 5 km on Etna, and 5 cm in the experiments. See text for further details.

parallel to it matches the position of the Gravina fault. Although experiments 7 and 11 (top and middle right, Fig. 7) reproduce the three systems reasonably correctly, experiment 8 (Fig. 7 lower left) has an additional fault, marked ? that has not been observed on Etna, though one section of it (marked N) where it is joined to the north by a north-south fault F does resemble the Nizzetti fault in position and orientation, where it is joined by the southward extension of the Fiandaca-Pennisi Faults. Models 7, 8 and 11 all show almost N-S structures branching north from the Tregastagni fault in its upper reaches. These do not correspond to known faults, but there are a couple of undated fissure eruptions oriented in this direction south of Monte Ilice and Monte Gorna, that may have exploited past faults here.

Like their counterparts on Etna, all three of these faults show distinct right lateral motion during the lifetime of each experiment. This is particularly well visible in the end state of experiment 7 (middle right Fig. 7), where the less pronounced north-south faults crossing each of them have been clearly displaced right-laterally. Again, their functioning seems to be identical to the corresponding trio of faults on Etna: similar to the Pernicana fault in the north, they mark the boundary between the relatively stationary western sector of the flanks where downslope and spreading motion are of similar magnitude and cancel each other out, and the rapid surface motion on the eastern side, where spreading and downslope sliding motion are summed.

In all of the models, these faults develop initially from fractures on the south slopes of the sand cones, which appear quickly soon after the start. These fractures then spend a much longer time gradually propagating southeastwards in the later stages of the experiment. In the picture of Experiment 12 after 50 min (Fig. 7 upper left), an analogue of the Trecastagni fault is starting to develop, but a Mascalucia-Tremestieri analogue has a long way still to go, and there is no clear sign of an analogue of the Gravina fault. On Etna, all faults on the summit cone or close to it have a higher chance of being buried under recent lavas or ash

falls, so may not be visible unless very recent.

4.1.6. Ragalna faults

Faulting of similar appearance and position to the Ragalna fault system is present in all but two of the experiments. In Fig. 7 these have been marked R. In the final phase of one of these simulations, experiment 7, this fault system has joined the Gravina fault to form a single curved fault marking the southwestern boundary of tectonic activity in the model. This is in line with the conclusions of Rust and Neri (1996), though it should be noted that this does not happen in experiments 7 or 11.

4.1.7. Western Graben

An equivalent structure to the Western Graben can be clearly seen in experiment 8 (Fig. 5), the northern part in experiments 6 and 13 (Fig. 6, marked W), and the southern part in experiment 7 (Fig. 7). In experiments 6 and 7 it is an extension of the Gravina fault, whereas in experiments 8 and 13 it joins with the Ragalna fault equivalent. It seems to be absent or ill-defined in experiments 9, 11 and 12.

4.2. Relative velocities of fault displacement in models and on Etna

Measurements of strike-slip displacement and extension were made across model faults that were well matched in shape and position to those of Etna. Two experiments, 7 and 11, gave good analogues of most of the major faulting systems so that comparative velocities throughout the model could be derived for each fault system.

Analogue model fault displacement was measured from the vertical scaled images taken throughout each experiment. The pepper sprinkled over the entire model at the start provided a unique pattern of reference points, and these could be found on each subsequent image. Points were selected from the final image either side of fractures, and distances between them measured. The same reference points were then found on the first image and the distance measured for this earlier time, the direction and amount of displacement then being divided by the time interval to provide a velocity. This was normally repeated for 2 to 4 nearby pairs of points and the average value taken, and also at 2 or 3 locations along fault.

The left-lateral displacement of analogues of the Pernicana fault was clearly visible in most experiments, and rates of slip ranged from 9 to 33 mm h^{-1}, with an average of 19.8 mm h^{-1}. These millimetres per hour values were converted to millimetres per year displacement velocities measured in the field on Etna (see above, sections 2.2 to 2.6), which are best represented by the value of 26 mm y^{-1} (Palano, 2016). Using the simple relation v_f / v_m, where v_f is the observed field strike-slip velocity of the Pernicana fault and v_m is the strike-slip velocity of its model counterpart gives a factor of x12000 model to field, which is used to scale the measurements of the other model fault systems in Table 3 and

Table 3
Measured displacement rates for model faults and their counterparts on Mt. Etna. Model values in mm y^{-1} are scaled up to Etna values in mm y^{-1} by using the Holocene values for the Pernicana fault strike slip rate as a standard, giving a conversion factor of x12000 model to Etna.

Model Fault	Type of Displacement	Exp 7	Exp 11	Exp 7	Exp 9	Exp 11	Exp 13	Mean Raw	Mean model values scaled	Etna field	period of time	References
		Last 191 m	Last 19 m	First 46 m		Last 44 m		mm h^{-1}	mm y^{-1}	mm y^{-1}		
Summit graben opening north	extension	5.9		17.4		22.7		20.0	27.2	229	1980–2018	Murray, 2019
Summit graben opening south	extension			16.9		24.5		20.7	28.2	179	1980–2018	
Mean Summit Graben	**extension**							**20.4**	**27.7**	**204**	±25	
Pernicana: Monte Pizzillo	left-lateral						18.8	18.8	25.6	26 ± 5	1874–1996	Garduño et al., 1997
Pernicana: Piano Provenzana	left-lateral									27 ± 7	13,700 y	Tibaldi and Gropelli, 2002
Pernicana: Mareneve	left-lateral	9.1	27.9	21.6	15.5	17.3		18.3	24.9	19	pre 2002	Neri et al., 2004
Pernicana: Presa	left-lateral		33.2	17.6	15.0	21.4	19.8	21.4	29.1	26	1999–2015	Palano, 2016
Mean Pernicana	**Left-lateral**							**19.8**	**27.0**	**27.0**	±9	
Trecastagni: at Trecastagni	Right lateral	5.0	13.5	1.3		6.2		6.5	8.8	2 to 5	1993–1997	Froger et al., 2001, Ranvier, 2004
Trecastagni: at Catania plain	Right lateral	3.3	10.6	5.4		6.0		6.3	8.6			Azzaro et al., 2013
Mean Trecastagni	**Right-lateral**							**6.4**	**8.7**	**3.5**	±2	
Mascalucia-Tremestieri: at Tremestieri	Right lateral	4.0	4.7	3.4		4.3		4.1	5.6	8 to 10	1993–1997	Froger et al., 2001, Ranvier, 2004, Bonforte et al., 2011
Mascalucia-Tremestieri: at Catania plain	Right lateral	3.2	6.8	3.6		9.4		5.7	7.8	15	1995–2000	Bonforte et al., 2011
Mean Mascalucia-Tremestieri	**Right-lateral**							**4.9**	**6.7**	**9**	±4	
Gravina: near Gravina	Right lateral	3.1	10.9	0.0		5.4		4.9	6.6	8 to 15	1993–2000	Froger et al., 2001, Ranvier, 2004, Bonforte et al., 2011
Gravina: at Catania plain	Right lateral	2.9	7.9	1.1		5.8		4.4	6.0	5	1995–2000	Bonforte et al., 2011
Mean Gravina	**Right-lateral**							**4.6**	**6.3**	**11.5**	±6	
Ragalna: north	extension		2.9					2.9	4.0		1999–2005	Neri et al., 2007
Ragalna: south	extension	2.6	2.1	0.8		1.9		1.8	2.5	3.5 to 4	1999–2005	Neri et al., 2007
Ragalna: south	Right-lateral	1.7		1.3		1.6		1.5	2.1	4 to 5	1999–2005	Neri et al., 2007
Mean Ragalna	**Right-lateral**							**1.5**	**2.1**	**4.5**	±0.5	
Mean Ragalna	**extension**							**2.0**	**2.8**	**3.8**	±0.3	

the rest of this section. This scaling ratio is roughly similar to that calculated from the model/nature viscosity, stress and length parameters, even with the large uncertainties possible in natural viscosity and stress estimates.

The images of the three parallel model faults similar to the Trecastagni, the Mascalucia-Tremestieri and the Gravina fault were also measured (Fig. 7). Model faults simulating the Trecastagni fault gave scaled right-lateral strike-slip velocities of 4.6 to 8.5 mm y^{-1}, which compare with 2 to 5 mm y^{-1} for the Trecastagni fault itself. In both model and field measurements, these values are lower than those of the Pernicana fault displacement velocity. Scaled displacement values for the model Mascalucia-Tremestieri fault are slightly larger at 4.9 to 9.6 mm y^{-1}, as are field values of 8 to 15 mm y^{-1}. Analogues of the Gravina fault, the most southerly of the three, showed different scaled strike-slip velocities between models, varying from no detectable slip to 7.9 mm y^{-1}. Field displacement measurements of the Gravina fault itself also varied, from 5 to 15 mm y^{-1}.

Model analogues of the main north-south faults of the Ragalna fault system provided measurements of both extension across the fault and right-lateral strike-slip where this was detectable. Scaled extension varied between 1 and 2.6 mm y^{-1}, and strike-slip from 0 to 1.7 mm y^{-1}. Field measurements of extension were between 3.5 and 4 mm y^{-1}, and strike-slip 4 to 5 mm y^{-1}.

The sum of the mean velocities of the three southern right-lateral transcurrent faults in the models totals 21.7 mm y^{-1}; or 23.8 mm y^{-1} if the western (corresponding to Ragalna) fault is included. This compares to field measurements totalling 24 mm y^{-1}, or 28.5 mm y^{-1} including the Ragalna faults. It is interesting that both model and field values summed are close to those of the Pernicana fault and its equivalent in the north, emphasising the point made earlier that the three or four southern faults fulfil the same function as the Pernicana fault in the north, with the strain release being distributed between three or four faults instead of one.

The extension across the north-south summit graben, visible across the sand cone of every experiment, was difficult to measure in many cases because the cone became broken up by the faulting, making reference points impossible to locate in successive images. Two models, 7 and 11, could be used, which gave scaled extension rates of 27 and 28 mm y^{-1}, of similar order to the Pernicana fault analogues. By contrast, the summit graben of Etna shows long term extension 1980–2018 of 179 to 229 mm y^{-1}. This is an order of magnitude greater than the Pernicana fault, so the model summit graben have much smaller relative extension rates than on Etna. The measurements of each of the model faults described above are given in Table 3 below, and compared to measurements from their counterparts on Etna, with references to field measurements in each case.

In this table, none of the field measurements except the Pernicana fault and the summit graben cover a period of more than six years of cumulative movement, so may not be representative of annual rates measured over long periods of time. Despite this caveat, in general there is a similar picture of distribution of velocities in the various sectors of the volcano with one exception: the summit graben. The comparatively much higher rates of extension across the summit graben of Etna are doubtless due to the additional force of magma pressure from the persistent injection of dykes, mainly oriented north-south, as discussed below in section 5.2. All the clear-cut extension events across the graben occurred during the injection of new dykes at the start of fissure eruptions, when sudden increases of up to 4.42 m occurred during a single eruption (Murray, 2019). The magma pressure from dyke injection created narrow areas of surface uplift alongside the dykes, though in most cases these disappeared in subsequent subsidence events.

5. Discussion

5.1. Limitations of our approach

There are many limitations to the application of our experimental approach to the real situation on Etna. The volcanic edifice is built on basement topography that is not a simple sloping plane. The area northwest of the summit is a vast buried plateau 17 × 7 km, and the land sloping east of the summit contains broad valleys that run downslope (Ogniben, 1966; Branca and Ferrara, 2013). Also, the basement is made up of different rock units, each with its own different properties, rather than a layer of uniform thickness and material behaviour. The lava apron surrounding the Etna summit cone is also not of uniform thickness, but thins steadily away to nothing in distal regions, except to the east where it fills a prominent sub-Etnean valley (Branca and Ferrara, 2013). Neither is the summit cone of Etna conical, but elongated north-south due to the Northeast Rift and the Piano del Lago, and with the 5 km wide and 1 km deep valley of the Valle del Bove on its eastern side. Another major difference is that our models contain no equivalent of magma pressure, which clearly increases gravitational spreading at the summit in the long term (Murray, 2019). There is also the fact that the continuing activity and output of the volcano and consequent rebuilding of the summit cone during the structural evolution of its flanks is not represented in the model. Despite these limitations, the models do provide the general structural and lithological context of Etna, and thus a generalised understanding of the fault systems produced by the specific configuration. They provide the mechanics of the general framework, but not the intricate details, and below we describe various modifications that take into account some details, and produce better fits.

5.1.1. Basement topography representation

Attempts were made to mitigate the effects of some of these drawbacks in some of the models. Firstly, the fact that the basement beneath Etna is an almost level plateau to the northwest, but steeper on the east side with broad valleys running down to the sea (Fig. 5 of Branca and Ferrara, 2013) is represented in experiment 2 by a step on the east side of the sand cone. The silicone putty was allowed to flow off the eastern edge of the board representing the basement onto the bench below. This rather crude attempt to create slope change in a single step was not particularly successful, with less than half the Etna faults represented. In experiment 8, the basement board was curved so that the slope gradually increased eastward from about 1° to 3°, which is closer to the real situation on Etna. This produced a much better fit, with analogues of 80% of Etna faults appearing.

In experiment 7, the downslope valleys in sub-Etna topography were represented by slightly curving the basement board to make an east-west valley 7 mm deep. This experiment was also one of the most successful, with 94% of Etna fault systems represented in the model (Fig. 7). Four experiments were adapted to better correspond to the thinning of the lava apron away from the summit cone. Although still planar rather than conical, the surface of the sand apron was thinned to the east in experiments 10 and 11, and to the southeast in experiments 12 and 13. In experiment 13 the sand apron thins to zero in the southeast corner (equivalent to the position of Catania on Etna). These experiments had mixed success, with experiments 10 and 12 at 25% and 30%, but 11 and 13 both achieving analogues of over 60% of Etna faults (Figs. 6 and 7).

5.1.2. Representation of Etna's irregular summit cone

In three of the experiments, 10, 11 & 14, an elongated sand cone was created to better represent the present shape of Etna. These too had mixed success, but 11 and 14 both showed reasonable representations of 63% of the Etna faults.

5.1.3. Representation of the Valle del Bove

A major feature of Mt. Etna is the Valle del Bove, a 4 × 5 km steep-sided valley at the eastern foot of the summit cone, with debris avalanche deposits at its eastern end, whose origin is usually attributed to large gravitational slope failure at around 10,000 years ago (Calvari et al., 2004) or to preferential leaf graben formation on this unconstrained side (Merle and Borgia, 1996). Such a feature is visible in the early phases of experiment 7, though its orientation is a about 10° different clockwise from the Valle del Bove itself (Fig. 7). In experiment 14, a valley was scooped out of the sand to the east of the sand cone with a spoon after the experiment had been running for 30 min, to represent a late stage slope failure, but this has no discernable effect on fault formation.

5.2. Magma pressure and persistent dyke intrusion

Despite these drawbacks, it is clear that the configuration of most of the faults on Etna can be explained by the interaction of two processes alone: the gravitational spreading of the Etna summit cone (Murray, 2019) combined with the seaward sliding of the entire Etna massif down its sloping basement (Murray et al., 2018). But a third process, magma pressure, is required to explain the fact that the lateral east-west expansion of the summit graben of Etna exceeds that of the models by an order of magnitude. Further clues as to how gravitational and magmatic processes interrelate were mentioned in sections 4.1.1 and 4.1.2, where it was noted that some of the bounding faults of summit graben in the analogue experimental models are at similar positions and orientations to fractures formed during the 1947, 1983, 1985, 1989, 1991–3, 2001 and 2002 flank eruptions of Etna. This is good evidence that the combination of spreading and downslope sliding is controlling the position of future eruptive vents by creating fractures and weaknesses that become the paths of least resistance for later intruding magmas, not just for north-south eruptive fissures, but in other orientations as well. Similar ideas have been proposed by Neri et al. (2005) for the precursive movements prior to the 2002–2003 eruption, and by Pezzo et al. (2020) for the 2018 paroxysm. This assertion carries with it the implication that forecasting the location of future eruptive vents might be possible by GNSS monitoring of an array of stations in the summit region, to detect sectors where circumferential strain is increasing, and therefore likely to favour crack propagation and intrusion (Wadge, 1976).

The constant intrusion of radial dykes over time, particularly near the summit but including those that feed eruptions low down on the flanks, means that space must be found for these dykes (Walker, 1992). Such intrusions always exert magma pressure normal to the dyke, which persistently results in widening (Murray, 1990, 1994) that in turn results in overall expansion of the volcano. Magma pressure from the intrusions is therefore substantially augmenting extension velocity in a single feedback loop.

The addition of material at the cone summit whilst the experiment was continuing, to represent the persistent continuing output of the Etna, would have increased the mass of the summit cone, which in turn would have had the effect of increasing the gravitational spreading in the later stages of the experiment. This and the similar effects of magma pressure may have altered the configuration of some of the faults as a result, increasing the effects of spreading at the expense of the effects of sliding.

5.3. Regional tectonics; East flank instability

Regarding the effect of regional tectonism, it is true that the millennial fault displacements of those Sicilian faults that pass beneath the Etna summit and flanks must be continuing. An idea of how much these movements contribute to observed fault displacement at the surface may be gauged from field determinations of displacements around Etna, which vary from 0.9 to 1.4 mm y^{-1} for the Holocene (Valensise and Pantosti, 1992; Monaco et al., 1997; Stewart et al., 1993). They are therefore smaller than all the field-measured slip rates of the Etna fault systems, by up to two orders of magnitude. This is strong evidence that regional movements are minor effects, largely overwhelmed by the processes described in this paper.

The instability of the eastern flank has dominated thinking on the structure of Etna over the past three decades. The analogue modelling described in this paper provides a framework to understand this phenomenon. Fig. 4 shows a typical experiment at the start (left) and after 50 min (right). Gravitational spreading has been obstructed by the sand barrier to the north, west and south of the sand cone, but allowed to flow freely down the slope to the east. This dichotomy is emphasised by the fact that all westward spreading is upslope, where sliding and spreading are operating in contrary directions so tend to cancel each other out, whereas to the east of the cone, spreading and downslope motion are summed. The outcome has been the almost stationary regions all around the cone except eastward, in which direction progress over the ductile layer beneath has been rapid. The inevitable consequence has been arcuate faulting of the brittle sand apron to the northeast and south of the cone, tectonically cutting off an easterly mobile sector. This simple combination of events offers both a description and explanation of the rapid eastward movement of the eastern flanks of Etna, and the difference between this and the comparatively stable ground to the north and west, a dichotomy known as the east flank instability.

6. Conclusions

The structural faults on the summit and flanks of Mt. Etna volcano originate principally from the two processes of gravitational spreading and the sliding of the Etna massif down its sloping basement. As such, Etna behaves as a mountain built on foundations unable to support it. What happens in the upper magmatic system is controlled by this framework.

The Peloritani mountains obstruct the gravitational spreading of the Etna cone northwards, and the southeast end of this mountain range marks the end point of obstruction. The abrupt change between stationary ground to the north, and the rapid eastward movement to the south where downslope sliding is added to gravitational spreading of the cone, results in the creation of the Pernicana fault, whose left-lateral strike-slip movement has the highest average velocity of the flank fault displacements of Etna.

The three transcurrent faults southeast of Etna, the Trecastagni, Mascalucia-Tremestieri and Gravina faults, are the result of a similar situation, in which the low range of hills along the southern edge of Etna also obstructs spreading, but being nearly twice as far from the summit cone, the tectonic strain release is spread between three faults, whose right-lateral displacement is individually less than the Pernicana, but summed together they are of similar velocity.

Together, the Pernicana and these southern faults tectonically cut off the more stable regions southwest, west and north of the volcano from the mobile eastern sector, generally termed the east flank instability.

The Ragalna fault system has started to propagate from the foot of the summit cone in a similar way to the three southern transcurrent faults, but as yet has failed to reach as far, but may do so in the future.

The Timpe faults result from the extension created by the downslope sliding and spreading of the eastern flank, as well as the submarine instability of the Etnean continental margin. Their orientation is sensitive to local changes in spreading direction.

The summit graben of Etna is the product of gravitational spreading of the cone, producing leaf graben that are suppressed in the east-west direction by tension consequent upon downslope sliding, but augmented in the north-south direction.

The ability of simple non-magmatic analogue models to recreate all the Etnean faults is significant, in that it shows clearly that the faulting and deformation has its origin in gravity.

The additional process of the intrusion of magma is also controlled

by gravitational spreading and sliding, which creates the cracking and faulting that intruding magma later follows. It might therefore be possible to detect the location of future eruptive vents by monitoring of an array of geodetic stations in the summit region to detect sectors of increasing tensional strain.

Lateral magmatic pressure from intrusive episodes dominates extension velocities at the summit of Etna, increasing graben opening by an order of magnitude compared to the scaled velocities of the analogue models in a feedback loop. On the flanks, model velocities of fault displacement match field measurements from Etna, indicating the limited effects of magma pressure elsewhere.

The faulting provides the framework in which to understand other Etnean activity, notably the hazards of eruptions, earthquakes and landslides.

Declaration of Competing Interest

The authors declare that they have no known competing financial interests or personal relationships that could have appeared to influence the work reported in this paper.

Acknowledgements

We thank Dr. S. Caffo and also the Parco dell'Etna, Corpo Forestale, Aziende Foreste, Sindaco di Comune di Linguaglossa and the Osservatorio Astrofisico (Catania), for permission to work on their land. We thank Claudia Martino for assistance with the laboratory analogue modelling in 2018. The fieldwork was supported by the U.K. Natural Environment Research Council (1975-1980, 1987-8, 1996-7, and more recently, grants NER/A/S/2001/00686, NER/A/S/2002/00411, NER/A/S/2003/00105, NE/D001390/1 and NE/E007589/1); CNRS, France (1981-1986); NATO (1988-1991); and the EEC (1992-8). The NERC Geophysical Equipment Facility loaned GPS kits (loan Nos. 727, 776, 799, 825, 869, 898 and 929). The Authors are grateful to the two anonymous reviewers for their useful criticism and suggestions that improved our work.

References

Acocella, V., Neri, M., Norini, G., 2013. An overview of experimental models to understand a complex volcanic instability: Application to Mount Etna, Italy. J. Volcanol. Geotherm. Res. 251, 98–111.

Argnani, A., Mazzarini, F., Bonazzi, C., Bisson, M., Isola, I., 2013. The deformation offshore of Mount Etna as imaged by multichannel seismic reflection profiles. J. Volcanol. Geotherm Res. 251, 50–64.

Azzaro, R., Bonforte, A., Branca, S., Guglielmino, F., 2013. Geometry and kinematics of the fault systems controlling the unstable flank of Etna volcano (Sicily). J. Volcanol. Geotherm. Res. 5–15.

Azzaro, R., Bonforte, A., D'Amico, S.D., Guglielmino, F., Scarfì, L., 2020. Stick-slip vs. stable sliding fault behaviour: a case-study using a multidisciplinary approach in the volcanic region of Mt. Etna (Italy). Tectonophysics 790. https://doi.org/10.1016/j.tecto.2020.228554.

Bonaccorso, A., Bonforte, A., Guglielmino, F., Palano, M., Puglisi, G., 2006. Composite ground deformation pattern forerunning the 2004–2005 Mount Etna eruption. J. Geophys. Res. 111, B12207. https://doi.org/10.1029/2005JB004206.

Bonaccorso, A., Bonforte, A., Currenti, G., Del Negro, C., Di Stefano, A., Greco, F., 2011. Magma storage, eruptive activity and flank instability: inferences from ground deformation and gravity changes during the 1993-2000 recharging of Mt. Etna volcano. J. Volcanol. Geotherm. Res. 200, 245–254. https://doi.org/10.1016/j.volgeores.2011.01.001.

Bonaccorso, A., Currenti, G., Del Negro, C., 2013. Interaction of volcano-tectonic fault with magma storage, intrusion and flank instability: a thirty years study at Mt. Etna volcano. J. Volcanol. Geotherm. Res. 251, 127–136.

Bonforte, A., Puglisi, G., 2003. Magma uprising and flank dynamics on Mt. Etna volcano, studied by GPS data (1994–1995). J. Geophys. Res. 108 (B3), 2153–2162.

Bonforte, A., Bonaccorso, A., Guglielmino, F., Palano, M., Puglisi, G., 2008. Feeding system and magma storage beneath Mt. Etna as revealed by recent infation/deflation cycles. J. Geophys. Res 113. https://doi.org/10.1029/2007JB005334. B05406. 2008.

Bonforte, A., Gambino, S., Guglielmino, F., Obrizzo, F., Palano, M., Puglisi, G., et al., 2007. Ground deformation modeling of flank dynamics prior to the 2002 eruption of Mt. Etna. Bull. Volcanol. 69, 757–768. https://doi.org/10.1007/s00445-006-0106-1.

Bonforte, A., Guglielmino, F., Coltelli, M., Ferretti, A., Puglisi, G., 2011. Structural assessment of Mount Etna volcano from permanent scatterers analysis. Geochem. Geophys. Geosyst. 12 https://doi.org/10.1029/2011GC003213.

Borgia, A., 1994. Dynamic basis of volcanic spreading. J. Geophys. Res. 99, 17,791–17,804.

Borgia, A., Ferrari, L., Pasquarè, G., 1992. Importance of gravitational spreading in the tectonic and volcanic evolution of Mount Etna. Nature 357, 231–235.

Bousquet, J.C., Lanzafame, G., 2004. The tectonics and geodynamics of Mt. Etna: synthesis and interpretation of geological and geophysical data. In: Bonaccorso, A., Calvari, S., Coltelli, M., Del Negro, C., Falsaperla, S. (Eds.), Etna Volcano Laboratory. American Geophysical Union (Geophysical monograph series), pp. 29–47.

Branca, S., Ferrara, V., 2013. The morphostructural setting of Mount Etna sedimentary basement (Italy): implications for the geometry and volume of the volcano and its flank instability. Tectonophysics 586, 46–64.

Branca, S., Coltelli, M., Groppelli, G., Lentini, F., 2011a. Geological map of Etna volcano, 1:50,000 scale. Ital. J. Geosci. 130 (3), 265–291. https://doi.org/10.3301/IJG.2011.15.

Branca, S., Coltelli, M., Groppelli, G., 2011b. Geological evolution of a complex basaltic stratovolcano: Mount Etna, Italy. Ital.J.Geosci. (Boll.Soc.Geol.It.) 130 (3), 306–317. https://doi.org/10.3301/IJG.2011.13.

Branca, S., De Beni, E., Chester, D., Duncan, A., Lotteri, A., 2017. The 1928 eruption of Mount Etna (Italy): reconstructing lava flow evolution and the destruction and recovery of the town of Mascali. J. Volcanol. Geotherm. Res. Volgeo 2017. https://doi.org/10.1016/j.jvolgeores.2017.02.002.

Bruno, V., Mattia, M., Montgomery-Brown, E., Rossi, M., Scandura, D., 2017. Inflation leading to a Slow Slip Event and volcanic unrest at Mount Etna in 2016: Insights from CGPS data. Geophys. Res. Lett. 44 https://doi.org/10.1002/2017GL075744, 12,141–12,149.

Calvari, S., Tanner, L.H., Groppelli, G., Norini, G., 2004. A comprehensive model for the opening of the Valle del Bove depression and hazard evaluation for the eastern flank of Etna volcano. In: Bonaccorso, A., Calvari, S., Coltelli, M., Del Negro, C., Falsaperla, S. (Eds.), Mt. Etna: volcano laboratory American Geophysical Union, Geophysical Monograph, 143, pp. 65–75.

Chiocci, F.L., Coltelli, M., Bosman, A., Cavallaro, D., 2011. Continental margin large-scale instability controlling the flank sliding of Etna volcano. Earth Planet. Sci. Lett. 305, 57–64.

Civico, R., Pucci, S., Nappi, R., Azzaro, R., Villani, F., Pantosti, D., Cinti, F.R., Pizzimenti, L., Branca, S., Brunori, C.A., Caciagli, M., Cantarero, M., Cucci, L., D'Amico, De Beni, E., De Martini, P.M., Mariucci, M.T., Montone, P., Nave, R., Ricci, T., Sapia, V., Smedile, A., Tarabusi, G., Vallone, R., Venuti, A., 2019. Surface ruptures following the 26 December 2018, Mw 4.9, Mt. Etna earthquake, Sicily (Italy). J. Maps 15 (2), 831–837. https://doi.org/10.1080/17445647.2019.1683476.

Cristofolini, R., Fichera, R., Patané, G., 1981. Osservazioni morfotettoniche sul settore occidentale dell'Etna. Geogr. Fis. Din. Quat. 4, 55–63.

De Beni, E., Branca, S., Coltelli, M., Groppelli, G., Wijbrans, J., 2011. Ar39/Ar40 isotopic dating of Etna volcanic succession. It. J. Geosci. (Boll. Soc. Geo. It.) 130 (3), 292–305. https://doi.org/10.3301/IJG.2011.14.

Delcamp, A., van Wyk de Vries, B., James, M., Gailler, L., Lebas, E., 2011. Relationships between volcano gravitational spreading and magma intrusion. Bull. Volcanol. 74, 743–765. https://doi.org/10.1007/s00445-011-0558-9.

Ferruci, F., Patané, D., 1993. Seismic activity accompanying the outbreak of the 1991-1993 eruption of Mt. Etna (Italy). J. Volcanol. Geotherm. Res. 57, 125–135.

Ferruci, F., Rasá, R., Gaudiosi, G., Azzaro, R., Imposa, S., 1993. Mt Etna: a model for the 1989 eruption. J. Volcanol. Geotherm. Res. 56, 35–56.

Froger, J.-L., Merle, O., Briole, P., 2001. Active spreading and regional extension at Mount Etnaimaged by SAR interferometry. Earth Planet. Sci. Lett. 187 (2001), 245–258.

Galland, O., Holohan, E., van Wyk de Vries B., Burchardt S., 2015. Laboratory modelling of volcano plumbing systems: a review. In: Breitkreuz, C., Rocchi, S. (Eds.), Physical Geology of Shallow Magmatic Systems. Advances in Volcanology (An Official Book Series of the International Association of Volcanology and Chemistry of the Earth's Interior). Springer, Cham. https://doi.org/10.1007/11157_2015_9.

Gambino, S., Cannata, A., Cannavò, F., La Spina, A., Palano, M., Sciotto, M., Spampinato, L., Barberi, G., 2016. The unusual 28 December 2014 dike-fed paroxysm at Mount Etna: timing and mechanism from a multidisciplinary perspective. J. Geophys. Res. Solid Earth 121, 2037–2053. https://doi.org/10.1002/2015JB012379.

Garduño, V.H., Neri, M., Pasquarè, G., Borgia, A., Tibaldi, A., 1997. Geology of the NE-Rift of Mount Etna (Sicily, Italy). Acta Vulcanol. 9, 91–100.

Grindley, G.W., 1973. Structural control of volcanism at Mount Etna. Phil. Trans. R. Soc. Lond. A. 274, 165–175.

Groppelli, G., Tibaldi, A., 1999. Control of rock rheology on deformation style and slip-rate along the active Pernicana Fault, Mt. Etna, Italy. Tectonophysics 305, 521–537.

Gross, F., Krastel, S., Geersen, J., Behrmann, J.H., Ridente, D., Chiocci, F.L., et al., 2016. The limits of seaward spreading and slope instability at the continental margin offshore Mt Etna, imaged by high-resolution 2D seismic data. Tectonophysics 667, 63–76.

Lo Giudice, E., Rasà, R., 1992. Very shallow earthquakes and brittle deformation in active volcanic areas: the Etnean region as an example. Tectonophysics 202, 257–268.

Lo Giudice, E., Patanè, G., Rasá, R., Romano, R., 1982. The structural framework of Mt Etna. Mem. Soc, Geol. It. 23, 125–158.

Merle, O., 2015. The scaling of experiments on volcanic systems. Front. Earth Sci. 3 https://doi.org/10.3389/feart.2015.00026.

Merle, O., Borgia, A., 1996. Scaled experiments of volcano spreading. J. Geophys. Res. 101, 13,805–13,817.
Merle, O., Lénat, J.-F., 2003. Hybrid collapse mechanism at Piton de la Fournaise volcano, Reunion Island, Indian Ocean. J. Geophys. Res. 108 (B3), 2166. https://doi.org/10.1029/2002JB002014.
Monaco, C., Tapponnier, P., Tortorici, L., Gillot, P.Y., 1997. Late Quaternary slip rates on the Acireale–Piedimonte normal faults and tectonic origin of Mt. Etna (Sicily). Earth Planet. Sci. Lett. 147, 125–139.
Murray, J.B., 1990. High-level magma transport at Mt Etna volcano, as deduced from ground deformation measurements. Chapter 17 of Magma Transport & Storage, Ed. Ryan. John Wiley & Sons Ltd., pp. 357–383
Murray, J.B., 1994. Elastic model of the actively intruded dyke feeding the 1991-1993 eruption of Mt Etna, derived from ground deformation measurements. Acta Vulcanol. 4, 97–99.
Murray, J.B., 2019. The cryptic summit graben of Mt Etna volcano. J. Volcanol. Geotherm. Res. 387 https://doi.org/10.1016/j.jvolgeores.2019.07.024.
Murray, J.B., Voight, B., Glot, J.-P., 1994. Slope movement crisis on the east flank of Mt Etna volcano: Models for eruption triggering and forecasting. Eng. Geol. 38, 245–259.
Murray, J.B., van Wyk de Vries, B., Pitty, A., Sargent, P.T.H., Wooller, L.K., 2018. Gravitational sliding of the Mt. Etna massif along a sloping basement. Bull. Volcanol. 80, 40. https://doi.org/10.1007/s00445-018-1209-1.
Neri, M., Acocella, V., Behncke, B., 2004. The role of the Pernicana Fault System in the spreading of Mount Etna (Italy) during the 2002–2003 eruption. Bull. Volcanol. 66, 417–430. https://doi.org/10.1007/s00445-003-0322-x.
Neri, M., Acocella, V., Behncke, B., Maiolinoa, V., Ursinoa, A., Velardita, R., 2005. Contrasting triggering mechanisms of the 2001 and 2002–2003 eruptions of Mount Etna (Italy). J. Volcanol. Geotherm. Res. 144, 235–255.
Neri, M., Guglielmino, F., Rust, D., 2007. Flank instability on Mount Etna: radon, radar interferometry, and geodetic data from the southwestern boundary of the unstable sector. J. Geophys. Res. 112, B04410. https://doi.org/10.1029/2006JB004756.
Obrizzo, F., Pingue, F., Troise, T., De Natale, G., 2001. Coseismic displacements and creeping along the Pernicana fault (Etna, Italy) in the last 17 years: a detailed study of a tectonic structure on a volcano. J. Volcanol. Geotherm. Res. 109, 109–131.
Ogniben, L., 1966. Lineamenti idrogeologici dell'Etna. Rivista Mineralogica Siciliana XVII N.100–102, 151–174.
Palano, M., 2016. Episodic slow slip events and seaward flank motion at Mt. Etna volcano (Italy). J. Volcanol. Geotherm. Res. 324, 8–14. https://doi.org/10.1016/j.jvolgeores.2016.05.010.
Palano, M., Aloisi, M., Amore, M., Bonforte, A., Calvagna, F., Cantarero, M., Consoli, O., Guglielmino, F., Mattia, M., Puglisi, B., Puglisi, G., 2006. Kinematics and strain analyses of the eastern segment of the Pernicana fault (Mt. Etna, Italy) derived from geodetic techniques (1997-2005). Ann. Geophys. 49 (4–5), 1105–1117. https://doi.org/10.4401/ag-3103.
Pezzo, G., Palano, M., Tolomei, C., De Gori, P., Gambino, P., Chiarrabba, C., 2020. Flank sliding: a valve and a sentinel for paroxysmal eruptions and magma ascent at Mount Etna, Italy. Geology 48 (11), 1077–1082. https://doi.org/10.1130/G47656.1.
Puglisi, G., Briole, P., Bonforte, A., 2004. Twelve years of ground deformation studies on Mt. Etna volcano based on GPS surveys. In: Bonaccorso, A., Calvari, S., Coltelli, M., Del Negro, C., Falsaperla, S. (Eds.), Mt. Etna: Volcano Laboratory. AGU, Washington, D.C, pp. 321–341. Geophysical Monograph Series 143.
Ranvier, F., 2004. Modélisation numérique des mouvements de flanc de l'Etna (Sicile, Italie) mis en evidence par interférométrie radar. Thesis for Docteur d'Université, Université Blaise Pascal, France, 277 pp.
Rasá, R., Azzaro, R., Leonardi, O., 1996. Aseismic creep on faults and flank instability at Mt. Etna volcano. In: McGuire, W.J., Jones, A.P., Neuberg, J. (Eds.), Volcano Instability on the Earth and Other Planets, Geol. Soc. Spec. Publ, 110, pp. 179–192.
Rittmann, A., 1973. Structure and evolution of Mount Etna. Phil. Trans. R. Soc. Lond. A. 274, 5–16.
Rust, D., Neri, M., 1996. The boundaries of large scale collapse on the flanks of Mount Etna, Sicily. In: McGuire, W.J., Jones, A.P., Neuberg, J. (Eds.), Volcano Instability on the Earth and Other Planets, Geol. Soc. Spec. Publ, 110, pp. 193–208.
Solaro, G., Acocella, V., Pepe, S., Ruch, J., Neri, M., Sansosti, E., 2010. Anatomy of an unstable volcano from InSAR: Multiple processes affecting flank instability at Mt. Etna, 1994–2008. J. Geophys. Res. 115 (B10405), 1–21. https://doi.org/10.1029/2009JB000820.
Stewart, I.S., McGuire, W.J., Vita-Finzi, C., Firth, C., Holmes, R., Saunders, S., 1993. Active faulting and neotectonic deformation on the eastern flank of Mount Etna, Sicily. Z. Geomorph. N. E Suppl. -Bd. 94, 73–94.
Tibaldi, A., Gropelli, G., 2002. Volcano-tectonic activity along structures of the unstable NE flank of Mt. Etna (Italy) and their possible origin. J. Volcanol. Geotherm. Res. 115, 277–302.
Urlaub, M., Petersen, F., Gross, F., Bonforte, A., Puglisi, G., Guglielmino, F., Krastel, S., Lange, D., Kopp, H., 2018. Gravitational collapse of Mount Etna's southeastern flank. Sci. Adv. 4, eaat9700.
Valensise, G., Pantosti, D., 1992. A 125 kyr-long geological record of seismic source repeatability: the Messina Straits (Southern Italy) and the 1908 earthquake (Ms 7.5). Terra Nova 4, 472–483.
Villano, F., Pucci, S., Azzaro, R., Civico, R., Cinti, F.R., Pizzimenti, L., Venuti, A., 2020. Surface ruptures database related to the 26 December 2018, MW 4.9 Mt. Etna earthquake, southern Italy. Scientific Data 7, 42. https://doi.org/10.1038/s41597-020-0383-0.
Wadge, G., 1976. Deformation of Mt Etna 1971-1974. J. Volcanol. Geotherm. Res. 1, 237–263.
Walker, G.P.L., 1992. 'Coherent intrusion complexes' in large basaltic volcanoes-a new structural model. J. Volcanol. Geotherm. Res. 50, 41–54.
Wooller, L.K., van Wyk de Vries, B., Murray, J.B., Rymer, H., Meyer, S., 2004. Volcano spreading controlled by dipping substrata. Geology 32 (7), 573–576. https://doi.org/10.1130/G20472.